


# Pharmacological blockade of ASCT2-dependent glutamine transport leads to antitumor efficacy in preclinical models

Michael L Schulte<sup>1-3</sup>, Allie Fu<sup>1</sup>, Ping Zhao<sup>1</sup>, Jun Li<sup>1</sup>, Ling Geng<sup>1</sup>, Shannon T Smith<sup>1</sup>, Jumpei Kondo<sup>4</sup>, Robert J Coffey<sup>4-6</sup> , Marc O Johnson<sup>7</sup>, Jeffrey C Rathmell<sup>7</sup>, Joe T Sharick<sup>8</sup>, Melissa C Skala<sup>8,13</sup>, Jarrod A Smith<sup>9,10</sup>, Jordan Berlin<sup>5</sup>, M Kay Washington<sup>5,7</sup>, Michael L Nickels<sup>1-3</sup> & H Charles Manning<sup>1-3,5,8,11,12</sup>

The unique metabolic demands of cancer cells underscore potentially fruitful opportunities for drug discovery in the era of precision medicine. However, therapeutic targeting of cancer metabolism has led to surprisingly few new drugs to date. The neutral amino acid glutamine serves as a key intermediate in numerous metabolic processes leveraged by cancer cells, including biosynthesis, cell signaling, and oxidative protection. Herein we report the preclinical development of V-9302, a competitive small molecule antagonist of transmembrane glutamine flux that selectively and potently targets the amino acid transporter ASCT2. Pharmacological blockade of ASCT2 with V-9302 resulted in attenuated cancer cell growth and proliferation, increased cell death, and increased oxidative stress, which collectively contributed to antitumor responses *in vitro* and *in vivo*. This is the first study, to our knowledge, to demonstrate the utility of a pharmacological inhibitor of glutamine transport in oncology, representing a new class of targeted therapy and laying a framework for paradigm-shifting therapies targeting cancer cell metabolism.

Healthy mammalian cells sequester the amino acid glutamine through an evolutionarily redundant family of transporters expressed on the cell surface known as the solute carrier family of proteins (SLC)<sup>1</sup>. Alanine–serine–cysteine transporter 2 (ASCT2, encoded by gene *SLCIA5*) is a sodium-dependent solute-carrier protein responsible for the import of neutral amino acids and is the primary transporter of glutamine in cancer cells<sup>2</sup>. Elevated ASCT2 levels have been linked to poor survival in many human cancers, including lung<sup>3</sup>, breast<sup>4</sup>, and colon<sup>5</sup>. Furthermore, several studies have attributed signal transduction and oncogene expression with an increased demand for glutamine. For example, *MYC* is responsible for transcribing the machinery of glutaminolysis, including *SLCIA5* (ref. 6), and a link has also been established between oncogenic *RAS* and glutamine dependency in colon cancer<sup>7</sup> and lung cancer<sup>8</sup>.

The critical role of glutamine in cancer cell growth and homeostasis suggests potential for new therapies targeting glutamine metabolism; however, efforts thus far have been met with limited success<sup>9,10</sup>. One strategy currently being evaluated in early-phase clinical trials targets mitochondrial glutaminase (GLS1; CB-839 (Calithera Biosciences)), an enzyme responsible for converting glutamine to glutamate.

Although promising, a limitation of this strategy is that targeting GLS1 does not fully address the extra-mitochondrial roles of glutamine, which include *RAS*-independent activation of MAPK signaling<sup>11</sup>. We hypothesized that antagonizing cell-surface glutamine transport, which could potentially be capable of abrogating multiple facets of glutamine metabolism, may represent a more efficacious approach. In support of this hypothesis, prior genetic studies silencing ASCT2 in cancer cells resulted in dramatic antitumor effects<sup>4,12</sup>. Toward this end, we report development of V-9302, the first small molecule antagonist of a glutamine transporter, and evaluate its use in an oncology setting. Pharmacological blockade of ASCT2 with V-9302 resulted in attenuated cancer cell growth and proliferation, increased cell death, and increased oxidative stress, which collectively contributed to antitumor responses *in vitro* and in mouse models *in vivo*.

## RESULTS

Previously, we discovered a new series of small molecule glutamine-transport antagonists<sup>13</sup>. From this series of 2-amino-4-*bis*(aryloxybenzyl)aminobutanoic acids, a lead emerged (V-9302; **Fig. 1a**) that was found to be among the most potent inhibitors of live-cell glutamine

<sup>1</sup>Vanderbilt Center for Molecular Probes, Vanderbilt University Medical Center, Nashville, Tennessee, USA. <sup>2</sup>Vanderbilt University Institute of Imaging Science, Vanderbilt University Medical Center, Nashville, Tennessee, USA. <sup>3</sup>Department of Radiology and Radiological Sciences, Vanderbilt University Medical Center, Nashville, Tennessee, USA. <sup>4</sup>Department of Medicine, Vanderbilt University Medical Center, Nashville, Tennessee, USA. <sup>5</sup>Vanderbilt-Ingram Cancer Center, Vanderbilt University Medical Center, Nashville, Tennessee, USA. <sup>6</sup>Veterans Health Administration, Tennessee Valley Healthcare System, Nashville, Tennessee, USA. <sup>7</sup>Department of Pathology, Microbiology, and Immunology, Vanderbilt University Medical Center, Nashville, Tennessee, USA. <sup>8</sup>Department of Biomedical Engineering, Vanderbilt University, Nashville, Tennessee, USA. <sup>9</sup>Vanderbilt Center for Structural Biology, Vanderbilt University, Nashville, Tennessee, USA. <sup>10</sup>Department of Biochemistry, Vanderbilt University, Nashville, Tennessee, USA. <sup>11</sup>Department of Neurosurgery, Vanderbilt University Medical Center, Nashville, Tennessee, USA. <sup>12</sup>Department of Chemistry, Vanderbilt University, Nashville, Tennessee, USA. <sup>13</sup>Present address: Morgridge Institute for Research, Department of Biomedical Engineering, University of Wisconsin–Madison, Madison, Wisconsin, USA. Correspondence should be addressed to H.C.M. ([henry.c.manning@vanderbilt.edu](mailto:henry.c.manning@vanderbilt.edu)).

Received 12 January 2017; accepted 29 November 2017; published online 15 Jan 2018; doi:10.1038/nm.4464

uptake reported to date. As shown in **Figure 1b**, V-9302 inhibited ASCT2-mediated glutamine uptake in human cells in a concentration-dependent fashion and exhibited a 100-fold improvement in potency (V-9302 half-maximal inhibitory concentration ( $IC_{50}$ ) = 9.6  $\mu$ M) over  $\gamma$ -L-glutamyl-*p*-nitroanilide (GPNA;  $IC_{50}$  = 1,000  $\mu$ M)<sup>14</sup>, a previously reported inhibitor of glutamine uptake. Using a panel of <sup>3</sup>H-labeled amino acids that are transported by multiple transporter systems, including glutamine and other solutes not transported by ASCT2 (**Supplementary Fig. 1**), we observed that V-9302 preferentially inhibited glutamine transport at a concentration of up to tenfold greater than its  $IC_{50}$  (**Fig. 1c,d**). Similarly, V-9302 was found to be capable of inhibiting the uptake of another ASCT2 substrate, leucine (**Fig. 1d,e**), suggesting that its amino acid transport inhibitory profile was specific for ASCT2 but not restricted to glutamine. To confirm that V-9302 binds ASCT2, we employed the drug affinity responsive target stability (DARTS) technique<sup>15</sup> using HEK-293 cells expressing a tetracycline-inducible ASCT2 vector. The DARTS technique is a target-identification strategy that capitalizes upon reduction in protease susceptibility of a target protein upon drug binding<sup>15</sup>. We observed protection of ASCT2 from proteolysis in a V-9302-concentration-dependent manner (**Fig. 1f** and **Supplementary Fig. 2a**), indicating that there is a stable V-9302–ASCT2 interaction and therefore implying that ASCT2 is a putative V-9302 target. Interestingly, the ASCT2 paralog, ASCT1 (encoded by *SLC1A4*), was not stabilized in the presence of V-9302 (**Supplementary Fig. 2b**), suggesting that V-9302 exhibits ASCT2 selectivity.

### In silico modeling

To model points of interaction between V-9302 and ASCT2, we used an *in silico* homology model of human ASCT2 (hASCT2)<sup>16</sup>. We found that V-9302 was compatible with the orthosteric amino acid-binding pocket of hASCT2, which is localized within the trans-membrane region of the protein (**Fig. 2a**). The conserved  $\alpha$ -amino-acid headgroup of V-9302 appeared to form key interactions within the zwitterion recognition site (**Fig. 2b**), which has been shown through crystallographic data to recognize amino acids and derivatives thereof<sup>16</sup>. Similarly, docking glutamine into ASCT2 resulted in direct overlap with the putative binding pocket occupied by V-9302 (**Fig. 2c**). To validate the specific interactions observed, we performed an *in silico* alanine scan of residues located within the putative V-9302-binding pocket (**Fig. 2d**). The overall docking scores for binding pockets harboring p.S353A or p.D464A suggest strong corresponding side chain interactions at these residues (**Fig. 2d**). Consistent with results from the amino acid selectivity assay (**Fig. 1c,d**), V-9302 interactions with L-type amino acid transporter 1 (LAT1), another transporter of glutamine, suffered steric hindrance penalties (**Fig. 2e,f**). Interface scores for glutamine in ASCT2 and LAT1 were favorable in both models, whereas those for V-9302 were not (**Fig. 2f**). These two neutral amino acid transporters are frequently coexpressed and exhibit overlapping substrate specificity, which has led some to propose cooperatively between ASCT2 and LAT1 in certain cancers<sup>17,18</sup>.

### In vitro evaluation of V-9302

To evaluate the effects of V-9302 on human cancer cells, we conducted an *in vitro* efficacy screen of 29 human cancer cell lines spanning three tumor types (**Fig. 3a**). Given the anaplerotic nature of glutamine, we used an ATP-dependent assay of viability as a primary screen, which was validated in an independent follow-up screening. In the primary screen, we observed that V-9302 exposure reduced

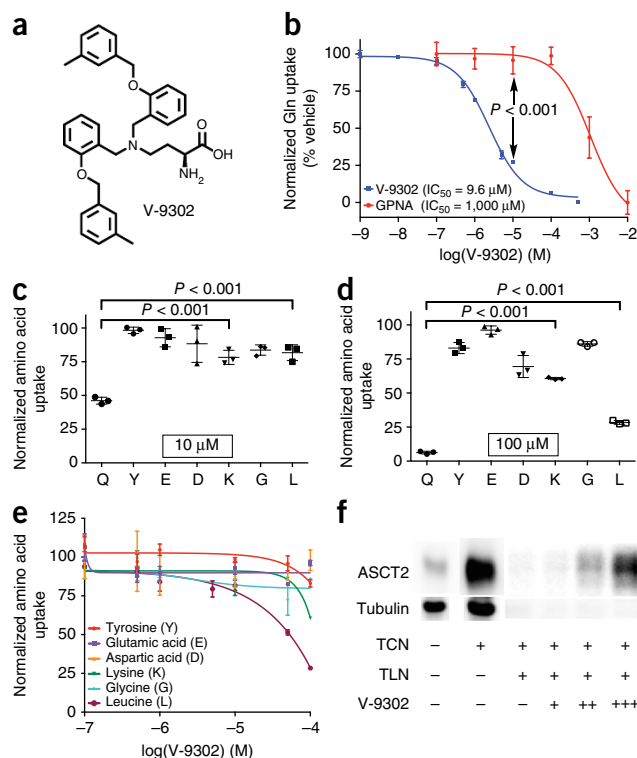


**Figure 1** V-9302 is an inhibitor of glutamine transport. **(a)** Chemical structure of V-9302. **(b)** Concentration-dependent inhibition of glutamine uptake in live HEK-293 cells.  $n = 3$  independent experiments performed in triplicate.  $P < 0.001$  at 10  $\mu$ M by Student's *t*-test. Cellular glutamine accumulation was normalized to that in cells exposed to vehicle. **(c,d)** Normalized amino acid uptake (relative to vehicle) in HEK-293 cells with V-9302 exposure at the  $IC_{50}$  (10  $\mu$ M, **(c)**) and at 10 $\times$  the  $IC_{50}$  (100  $\mu$ M, **(d)**) for glutamine inhibition.  $n = 3$  independent experiments.  $P < 0.001$  by Student's *t*-test. **(e)** Normalized uptake of <sup>3</sup>H-labeled amino acids in HEK-293 cells evaluated in the presence of increasing concentrations of V-9302.  $n = 3$  independent experiments. Normalization is relative to uptake in vehicle-injected controls. **(f)** DARTS assay visualized by immunoblot of tetracycline (TCN)-inducible ASCT2-expressing HEK-293 cells. ASCT2 is protected from proteolytic degradation by thermolysin (TLN) in the presence of increasing concentrations of V-9302 (-, vehicle; +, 50  $\mu$ M; ++, 100  $\mu$ M; +++, 200  $\mu$ M). Uncropped gel images are provided in **Supplementary Figure 21**. Error bars represent  $\pm$ s.d., and midlines represent means.

*in vitro* viability by at least 20% in more than half of the cell lines screened, with sensitivity to V-9302 exposure not obviously linked to select mutational status (**Supplementary Fig. 3**). Follow-up screening was carried out in a subset of colorectal cancer (CRC) cell lines that exhibited variable sensitivities to V-9302 in the primary screen. Using three independent assays lacking ATP dependency, we confirmed that V-9302 exposure led to reduced cellular viability and increased cell death (**Supplementary Fig. 4**)<sup>19</sup>. Although V-9302 impacted either viability or cell death to varying degrees across the panel of cell lines screened, certain particularly sensitive cell lines, including RKO, SW620, and LIM2537, exhibited dramatically decreased viability and increased cell death. To elucidate biological correlates of V-9302 sensitivity, we compared cell line sensitivity with ASCT2 levels (**Supplementary Fig. 5**) as well as viability in media depleted of ASCT2 substrates (**Supplementary Fig. 6**). Neither membrane-associated nor total ASCT2 levels correlated with V-9302-dependent changes in viability. However, cell lines sensitive to V-9302

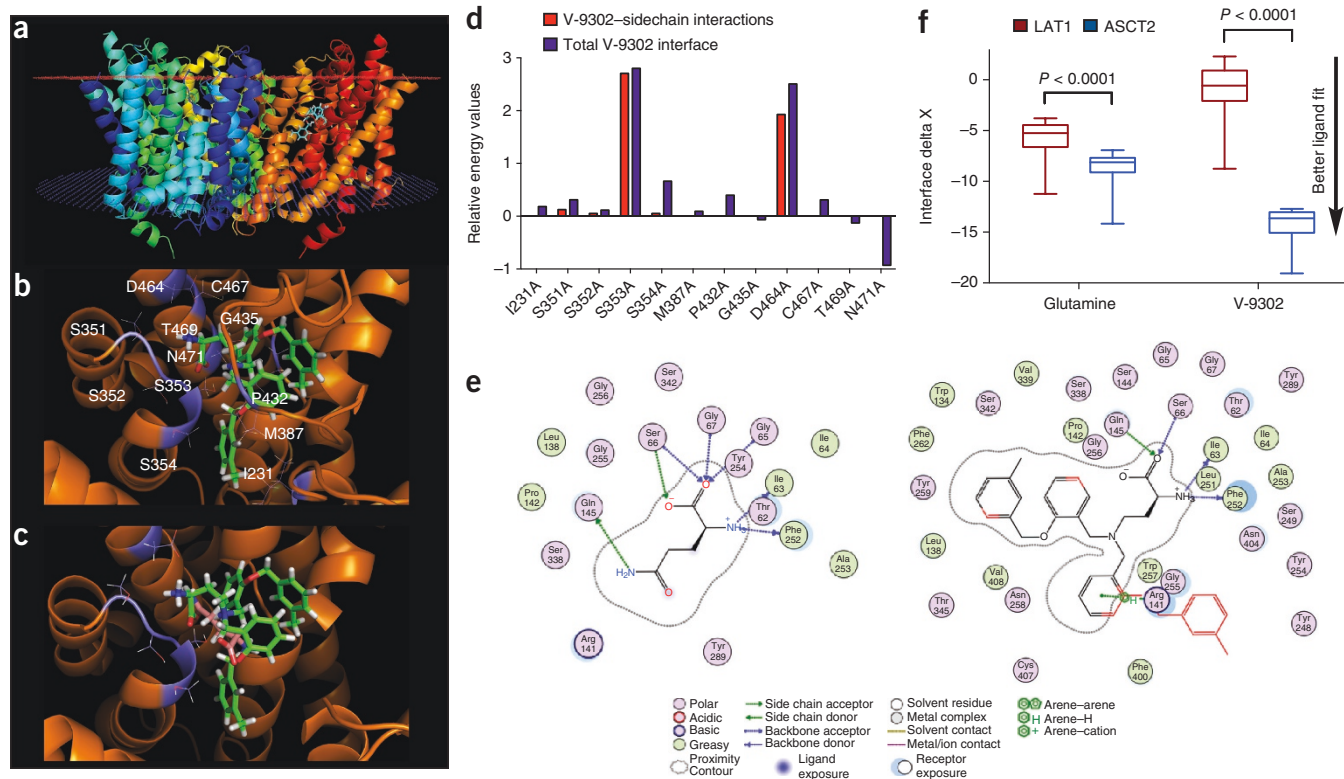


**Figure 2** *In silico* modeling of V-9302 interactions with hASCT2. (a) A homology model of hASCT2 (trimer shown) with V-9302 docked into the orthosteric binding site within the transmembrane region of the protein (red plane, extracellular membrane; blue plane, intracellular membrane). (b) Expanded view of the residues proximal to V-9302 within the orthosteric binding site. The top-scoring pose (predicted to have the lowest energy and thus most predictive of the binding mode of V-9302) is shown. (c) Overlay of V-9302 and the ASCT2 substrate glutamine docked into the orthosteric binding site. (d) *In silico* alanine scan of the hASCT2 binding pocket with the indicated variants. Positive values indicate that the alanine substitution interacts less favorably with V-9302 than the native residue. The total interface score is a weighted summation of the hydrogen-bonding scores, repulsion penalties, solvation energies, and electrostatic potential. Glutamine and V-9302 were evaluated in a homology model of LAT1. (e) Ligand interaction diagram of glutamine or V-9302 in LAT1 visualized in the Molecular Operating Environment (MOE) molecular modeling and simulation package. Steric clash with the surrounding residues is indicated in red (only seen with V-9302). (f) Docking scores for glutamine and V-9302 into LAT1; a similar fit was observed for glutamine in LAT1 and ASCT2, although V-9302 only fits the ASCT2 binding pocket.  $n = 100$  top-scoring poses per condition.  $P$  values were determined by Student's  $t$ -test. For box plots, the center line is plotted at the median; the box spans from the first quartile to the third quartile; and whiskers represent the minimum to maximum.

exposure exhibited reduced viability and increased cell death when propagated in glutamine- or ASCT2-substrate-depleted media. Finally, we examined cellular viability after exposure to V-9302 or CB-839 in four human CRC cell lines (Fig. 3b). The half-maximal effective concentration ( $EC_{50}$ ) for the four CRC cell lines exposed to V-9302 ranged from approximately 9–15  $\mu$ M, and CB-839 did not exhibit appreciable activity under identical conditions. Glutamine plays critical roles in T cell proliferation and activation<sup>20</sup>. We evaluated the effects of V-9302 on activated CD8<sup>+</sup> T cells *in vitro* and found T cell viability unchanged relative to that following vehicle treatment (Supplementary Fig. 7a). T cell activation was also not impaired after V-9302 exposure (Supplementary Fig. 7b).

#### Determinants of response to V-9302

To elucidate determinants of the response to V-9302 *in vitro*, we carried out shRNA knockdown of ASCT2 in HCC1806 cells as previously shown<sup>4</sup>; this enabled direct comparison with results from silencing the target. Silencing of ASCT2 (Fig. 4a) and V-9302 exposure (Fig. 4b) in HCC1806 cells resulted in analogous downstream effects, including markedly decreased phosphorylated (p)-S6 levels and a modest decrease in p-ERK levels. A similar inhibitory profile was observed in V-9302-treated HT29 cells (Supplementary Fig. 8). Using an

independent biochemical assay for p-ERK activity, we validated that V-9302 exposure resulted in a statistically significant, concentration-dependent decrease in p-ERK that was not observed following CB-839 exposure in HCC1806 or HT29 cells (Supplementary Fig. 9). In addition, *in vitro* V-9302 exposure in HCC1806 cells at concentrations that exceeded the  $IC_{50}$  for glutamine uptake led to increased levels of oxidized glutathione (GSSG) at the expense of reduced glutathione (GSH; Fig. 4c) and a corresponding increase in intracellular reactive oxygen species (ROS; Fig. 4d). V-9302 exposure led to elevated GSSG levels and ROS in HT29 cells, which was similar to what occurred in HCC1806 cells, but these features were not observed following CB-839 exposure (Supplementary Fig. 10). Autophagy following V-9302 exposure was observed in multiple cell lines, which was not unexpected when considering the relationship between amino acid withdrawal, regulation of mechanistic target of rapamycin (mTOR), and autophagy<sup>18</sup>. Immunofluorescence analysis (Fig. 4e) revealed that V-9302 exposure in HCC1806 cells led to elevated expression of microtubule-associated protein 1 light chain 3B (LC3B), a marker of autophagy<sup>12</sup>. Autophagic flux was elevated with V-9302 exposure in a concentration-dependent manner in the HCC1806 cell line as well as the HT29 cell line (Supplementary Fig. 11a,b). Combining V-9302 with the lysosomal inhibitor



chloroquine further increased the number of autophagic vesicles in HT29 cells (Supplementary Fig. 11b). In contrast, CB-839 exposure did not lead to elevated autophagic flux with or without the addition of chloroquine (Supplementary Fig. 11c). Combined exposure to chloroquine and V-9302 further decreased cell viability in HT29 and HCT-116 cells relative to that following exposure to a single agent or vehicle. In contrast, CB-839 did not decrease cell viability in these cell lines under identical conditions, nor did it exhibit a combinatorial effect with chloroquine (Supplementary Fig. 12a,b). In accordance with modulated oxidative stress and increased oxidation of NAD(P)H by glutathione reductase, V-9302 exposure led to a decreased optical oxidation–reduction (redox) ratio in HCC1806 cells (ratio of NAD(P)H to FAD; Fig. 4f)<sup>21</sup> and decreased the fluorescence lifetimes of both NAD(P)H and FAD (Supplementary Fig. 13). The optical redox ratio of a cell is well conserved and has been highly validated with independent measurements, including glycolytic activity and oxygen consumption. The changes in the optical redox ratio following V-9302 exposure, and their magnitude, are consistent with results from prior studies correlating these measures with inhibition of the PI3K–Akt–mTOR pathway in human breast cancer cells<sup>22</sup>. The efficacy of V-9302 was further evaluated in two CRC organoids developed at the Vanderbilt University Medical Center expressing activating mutations in *KRAS* and *BRAF*. The viability of both organoid A-007 (harboring *BRAF*-V600E) and organoid A-008 (harboring *KRAS*-G12V; p53-R248Q; PTEN-L140Y) was significantly reduced with exposure to V-9302 (Fig. 4g). In contrast, the same organoids were not significantly affected by CB-839 exposure (Supplementary Fig. 14).

### Evaluation of V-9302 *in vivo*

We next evaluated the performance of V-9302 *in vivo*. We first established that steady-state plasma concentrations were achieved at 4 h post-administration with a half-life of approximately 6 h in healthy mice (Supplementary Fig. 15). The effects of acute and chronic V-9302 exposure on plasma levels of glucose and glutamine were also evaluated in healthy mice. Following a single acute V-9302 exposure (4 h), plasma glucose levels in V-9302-treated mice were not significantly different from those in vehicle-treated controls, yet plasma glutamine levels were elevated by approximately 50%; this was likely a pharmacodynamic effect (Supplementary Fig. 16a,b). Plasma glucose levels between mice chronically exposed to V-9302 or vehicle over a 21-d regimen were not significantly different, whereas plasma glutamine levels were slightly decreased in the V-9302-exposed mice (Supplementary Fig. 16c,d). To evaluate the effect of V-9302 on glutamine levels in tumors, we employed noninvasive positron emission tomography (PET) imaging using [4-<sup>18</sup>F]fluoroglutamine<sup>5</sup>. Following a single dose of V-9302 (75 mg per kg body weight, 4 h), [<sup>18</sup>F]-4F-glutamine uptake in tumors in mice bearing HCC-1806 cell-line xenografts ( $n = 4$ ) was reduced by approximately 50%, reaching levels below background uptake in healthy muscle (Fig. 5a–c). Unlike what occurred in tumors, [4-<sup>18</sup>F]fluoroglutamine uptake in muscle was unaffected by V-9302 exposure (Fig. 5c), whereas [4-<sup>18</sup>F]fluoroglutamine uptake in liver was modestly elevated ( $P = 0.05$ , Student's *t*-test) following V-9302 treatment. We next carried out chronic-exposure studies in tumor-bearing mice. Athymic nude mice (Hsd: Athymic nude-Foxn1<sup>nu</sup>) bearing HCT-116 (*KRAS*-G13D) or HT29 (*BRAF*-V600E) cell line xenografts were treated with 75 mg V-9302 per kg body weight per day for 21 d. Over the treatment course, V-9302 prevented tumor growth as compared to vehicle

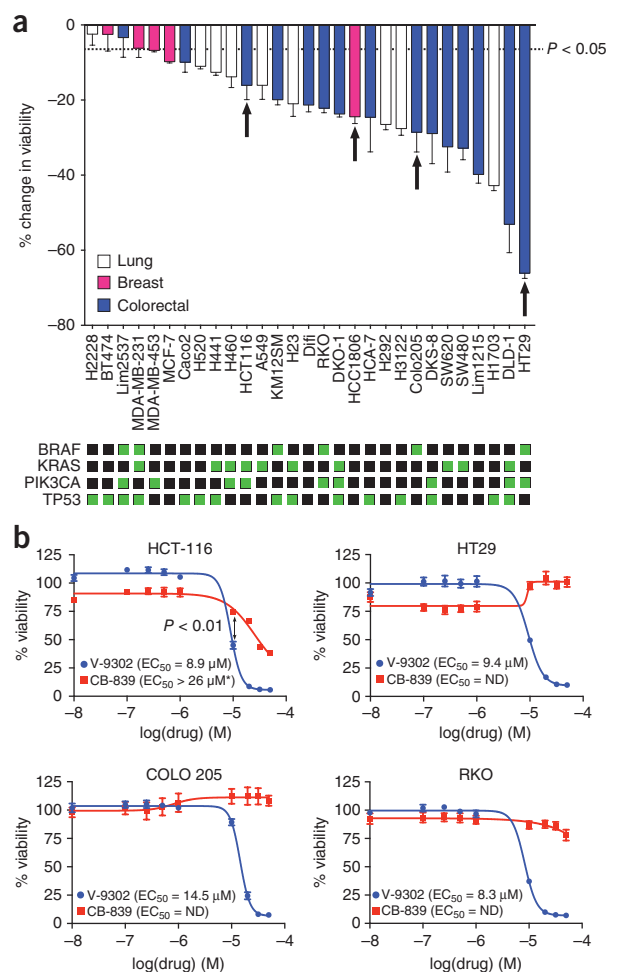


**Figure 3** *In vitro* efficacy of V-9302. (a) A panel of 29 human cancer cell lines were exposed to a single concentration of V-9302 (25  $\mu$ M, 48 h), and results from an assay of ATP-dependent viability following this exposure are shown. Select mutational status is highlighted (green squares). Cell lines derived from lung cancer (white bars), breast cancer (pink bars), and CRC (blue bars) are shown.  $n = 3$  independent experiments. Specific cell lines representing a range of *in vitro* sensitivities prioritized for further evaluation *in vivo* are indicated by arrows. Cell lines with  $P < 0.05$  by Student's *t*-test relative to vehicle control appear below the dotted line. (b) Direct comparison between the effect of V-9302 and CB-839 on the viability of human CRC cell lines. Cells were incubated with the indicated drugs at the concentrations shown for 48 h. Percent viability relative to that following vehicle exposure is shown.  $n = 3$  independent experiments. \*, the estimated  $EC_{50}$ .  $P < 0.01$  at 10  $\mu$ M by Student's *t*-test. Error bars represent  $\pm$ s.d. ND, not defined.

in both HCT-116 (Fig. 5d) and HT29 (Fig. 5f) xenograft models. Consistent with results from the *in vitro* mechanistic studies, V-9302 led to significantly decreased expression of p-S6 in tumor tissue in both HCT-116 (Fig. 5e) and HT29 (Fig. 5g) xenografts. In addition to decreased p-S6 IHC staining, V-9302 treatment led to elevated levels of cleaved caspase 3 in both HCT-116 (Fig. 5e) and HT29 (Fig. 5g) xenografts. To evaluate V-9302 in a more clinically relevant model, we conducted a similar chronic-exposure study in mice bearing a patient-derived xenograft (PDX) tumor (A-008: *KRAS*-G12V; p53-R248Q; PTEN-L140Y). Over the treatment course, V-9302 exposure led to a reduction in tumor volume as compared to vehicle exposure (Fig. 5h,i). To expand *in vivo* determinants of response to

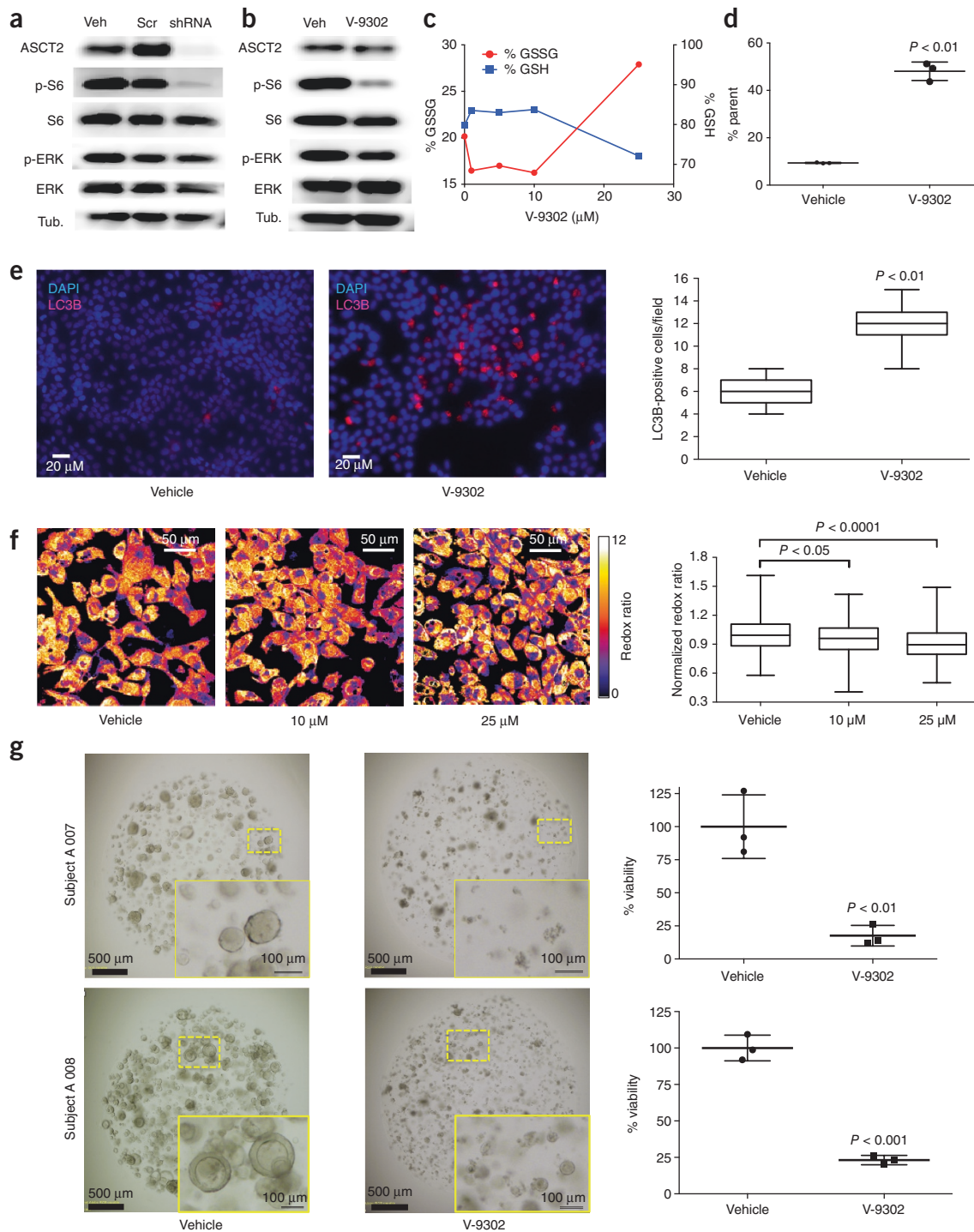


**Figure 4** Molecular determinants of ASCT2 antagonism *in vitro*. (a) Silencing ASCT2 (shRNA; HCC1806 cells; immunoblot shown) resulted in significantly attenuated p-S6 and modestly decreased p-ERK levels. (b) V-9302 exposure (25  $\mu$ M, 48 h) exhibited a similar inhibition profile to silencing ASCT2 with shRNA in HCC1806 cells. Uncropped gel images are provided in **Supplementary Figure 21**. (c, d) Graph showing the production of GSSG (left y axis) and depletion of GSH (right y axis) with V-9302 treatment in HCC1806 cells (c) and results from a corresponding assay of ROS (d).  $n = 3$  independent experiments.  $P < 0.01$  by Student's *t*-test. (e) Effect of V-9302 exposure (25  $\mu$ M, 48 h) on expression of LC3B, a marker of autophagy, in HCC1806 cells. Left, immunofluorescence photomicrographs showing cellular LC3B localization (pink fluorescence). Right, quantified numbers of LC3B<sup>+</sup> cells per field are shown.  $n = 3$  independent experiments.  $P < 0.01$  by Student's *t*-test. Magnification, 40 $\times$ . (f) Left, representative photomicrographs showing the effect of V-9302 exposure (10 or 25  $\mu$ M, 48 h) on the optical redox ratio (FAD/[NAD(P)H]) in HCC1806 cells. Right, corresponding quantification of the redox ratio.  $n = 3$  independent experiments.  $P$  values were determined by Student's *t*-test. Magnification, 40 $\times$ . (g) Left, representative bright-field photomicrographs showing the effects of V-9302 exposure (25  $\mu$ M, 96 h) on the viability of two human CRC organoids (A-007: BRAF-V600E; A-008: KRAS-G12V; p53-R248Q; PTEN-L140Y). Right, corresponding quantified organoid viability.  $n = 3$  independent experiments.  $P$  values were determined by Student's *t*-test. Error bars represent  $\pm$ s.d., and midlines represent means. For box plots, the center line is plotted at the median; the box spans from the first quartile to the third quartile; and whiskers represent the minimum to maximum.

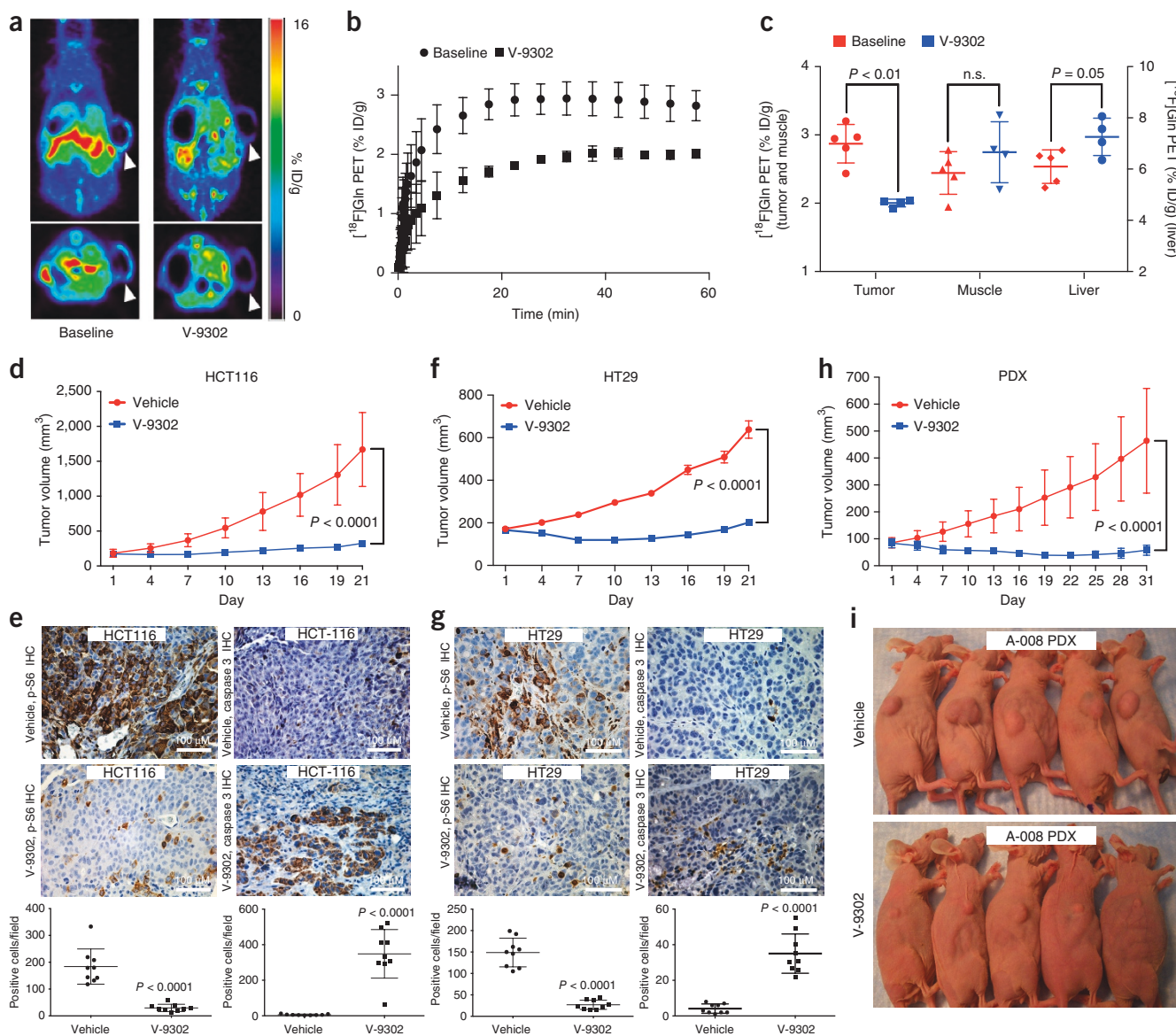


**Figure 5** Evaluation of V-9302 *in vivo*. (a) Pharmacodynamic [4-<sup>18</sup>F]fluoroglutamine PET imaging before and 4 h following a single administration of V-9302 (75 mg per kg body weight) in mice bearing xenografts from the HCC1806 cell line (arrows indicate xenograft tumor on right flank; central photopenia was observed). % ID/g, percentage of the injected dose per gram of tissue. (b) Mean time-activity curves (TACs) from tumor regions of interest ( $n = 4$  measurements per condition); data were collected before and 4 h following V-9302 administration. (c) Quantified tracer accumulation in xenograft tumors, muscle, and liver.  $n = 4$  measurements per condition.  $P$  values were determined by Student's  $t$  test. (d, f) Volumetric analysis over a 21-d treatment regimen (with vehicle or V-9302; 75 mg per kg body weight, daily) in athymic nude mice with HCT-116 (d) and HT29 (f) cell line xenografts.  $n = 10$  mice per group. Treatment started at 12 d following tumor injection for HCT-116 and at 4 d following injection for HT29.  $P$  values on day 21 were determined by Student's  $t$ -test. (e, g) Immunohistochemistry analysis showing p-S6 and caspase 3 in vehicle- or V-9302-treated HCT-116 (e) and HT29 (g) xenografts. Representative photomicrographs (top) and quantitation (bottom) are shown. Magnification, 20 $\times$ .  $P$  values were determined by Student's  $t$ -test. (h) Volumetric analysis over a 31-d treatment regimen (with vehicle or V-9302; 75 mg per kg body weight, daily) on athymic nude mice bearing PDX tumors (PDX A-008: F<sub>3</sub> generation, KRAS-G12V; p53-R248Q; PTEN-L140Y).  $n = 10$  mice per group. The  $P$  value on day 31 was determined by Student's  $t$ -test. (i) Photographs of A-008-PDX-bearing mice treated with V-9302 or vehicle at day 16 of 31. Error bars represent  $\pm$ s.d., and midlines represent means.

V-9302, we carried out a 10-d exposure study in athymic nude mice bearing HCC1806 or COLO 205 xenografts (Supplementary Figs. 17 and 18). Both models exhibited V-9302-dependent arrest of tumor growth analogous to that observed in HCT-116 and HT29 xenografts. Response to V-9302 in the HCC1806 xenografts was characterized by elevated levels of LC3B and cleaved caspase 3 along with decreased levels of p-Akt (Ser473) and p-S6 (Supplementary Fig. 17). Similarly, V-9302 treatment in COLO 205 xenografts led to

elevated levels of LC3B and cleaved caspase 3 and decreased levels of p-Akt (Ser473 and Thr308) as well as increased expression of cleaved poly(ADP-ribose) polymerase (PARP) and decreased p-ERK expression in COLO 205 xenografts (Supplementary Fig. 18). Additional insights into V-9302-mediated response in COLO 205 xenografts included decreased tumor bromodeoxyuridine (BrdU) uptake as well as elevated expression of p-glycogen synthase kinase 3 beta (GSK-3 $\beta$ ), p-proline-rich Akt substrate of 40 kDa (PRAS40), p38, and p53. Over



the course of the chronic-exposure studies, no substantial weight loss was observed in V-9302-treated cohorts relative to vehicle-treated controls (**Supplementary Fig. 19**). Additionally, liver pathology was similar among mice chronically treated with either V-9302 or vehicle (**Supplementary Fig. 20**).

To globally evaluate the *in vivo* effects of V-9302 on tumors, we carried out an unbiased metabolomics analysis of HT29 xenografts following 21 consecutive days of V-9302 exposure or vehicle treatment. A total of 782 metabolites of known identity that span 50 distinct metabolic pathways were quantitatively evaluated by liquid chromatography–mass spectrometry (LC–MS, Metabolon; **Supplementary Data 1**). Notably, V-9302 exposure significantly ( $P < 0.05$ , Welch's two-sample *t*-test) impacted 239 metabolites that spanned seven metabolic categories (**Fig. 6a**), each attributable to various aspects of ASCT2 transport and glutamine metabolism. Certain metabolites impacted by V-9302 treatment were directly downstream of ASCT2 transport, such as *N*-acetylserine, which was reduced in V-9302-treated tumors by greater than fourfold. Evidence of V-9302's impact on ATP included significantly reduced creatine phosphate levels in treated tumors. Levels of GSSG and 4-hydroxynonenal–glutathione were significantly elevated following V-9302 exposure, confirming earlier *in vitro* studies that identified oxidative stress as a key impact of V-9302 treatment. Other families of metabolites, including various nucleotide sugars, amino sugars, and metabolites within the pentose phosphate pathway<sup>23,24</sup>, were also elevated; this appeared to indicate a compensatory metabolic shift to glucose metabolism. Several metabolites impacted by V-9302 treatment were related to membrane biosynthesis and integrity. Numerous phospholipids, phosphatidylethanolamines, ceramides, and cholesterol metabolites, which are largely consistent with an autophagic fingerprint<sup>25–29</sup>, were modulated by V-9302 exposure.

## DISCUSSION

The diversity of metabolic pathways that cancer cells rely upon represents a key opportunity for drug development and precision medicine. It is well recognized that energy production in cancer cells is uniquely dependent upon specific nutrients, such as glucose and glutamine. Despite overwhelming evidence illuminating the prominent role of glutamine in cancer cell growth and homeostasis, few efforts have resulted in therapies capable of effectively antagonizing glutaminolysis thus far.

Mitochondrial glutaminase (GLS1), the enzyme responsible for catalyzing the conversion of glutamine to glutamate, represents a potentially promising target. Glutaminase is elevated in many tumors and tends to be associated with high-grade lesions<sup>30</sup>. Studies evaluating genetic silencing of GLS1 activity encouraged the development of GLS1 inhibitors<sup>31–33</sup>. One compound, CB-839 (Calithera Biosciences), is a selective GLS1 inhibitor now being explored clinically in multiple solid and liquid tumors<sup>10</sup>.

Here we report on V-9302, the first selective and potent small molecule antagonist of a glutamine transporter. We hypothesized that blocking cellular glutamine transport would impart a greater impact on glutamine metabolism in cancer cells than targeting downstream enzyme activity (for example, GLS1), particularly given the extensive biological plasticity leveraged by cancer cells to maintain intracellular glutamate pools. The new inhibitor V-9302 is distinct from investigational therapies targeting glutamine metabolism, as it is designed to abrogate all facets of glutamine signaling and metabolism downstream of ASCT2-mediated import. This differs dramatically from glutaminase inhibitors, which largely overlook the role of glutamine on MAPK signaling<sup>11</sup>, the activity of GLS2 (ref. 34), and the activity

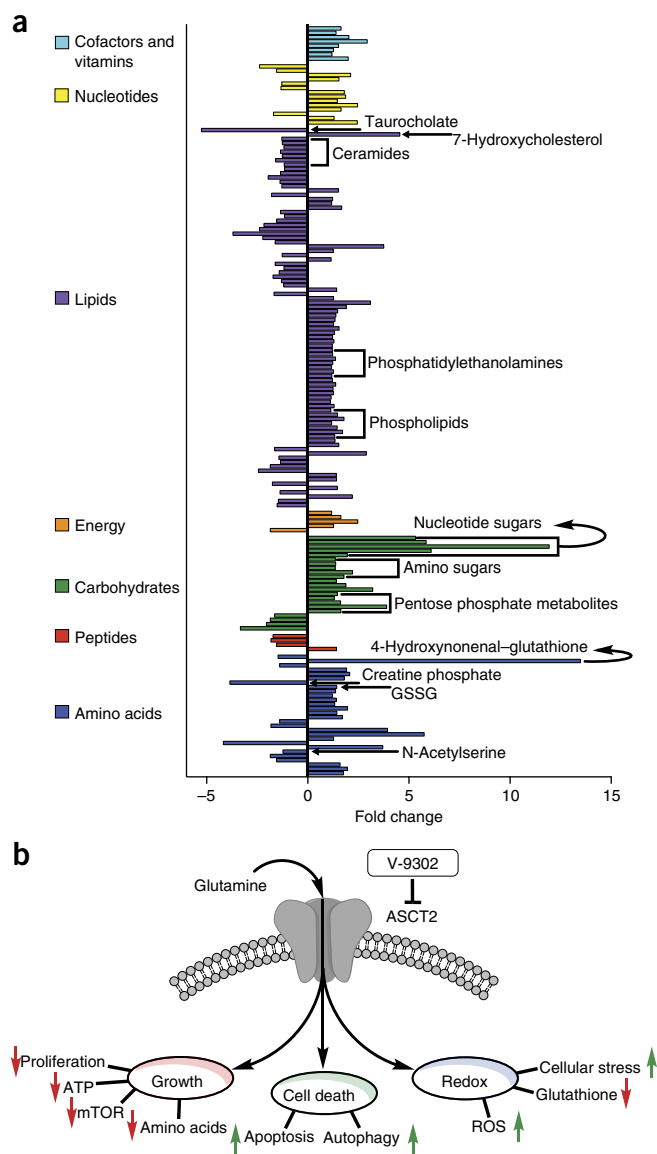


**Figure 6** Summary of cancer cell programs modulated by V-9302. (a) Global metabolomic analysis of mice bearing tumor xenografts from the HT-29 cell line treated with V-9302 or vehicle.  $n = 5$  mice per condition. Individual statistically significant ( $P < 0.05$  as determined by Welch's two-sample *t*-test) metabolites spanning seven distinct metabolic families are highlighted. Select metabolites are involved in glutamine-centric biological processes as indicated. (b) ASCT2 blockade with V-9302 results in attenuated cancer cell growth and proliferation, cell death, and oxidative stress. Arrows indicate V-9302-induced phenotypes relative to baseline homeostasis. Additional substrates transported by ASCT2 include alanine, serine, cysteine, threonine, leucine, and asparagine.

of amino acid transporters that require glutamine antiport for their function (for example, LAT1)<sup>18</sup>. Specifically antagonizing ASCT2, as shown in this study, results in another distinguishing feature of V-9302: the ability to block ASCT2-mediated transport of additional neutral amino acids beyond glutamine (**Fig. 6**). Although abrogation of cancer cell glutaminolysis represents a central motivation for the development of V-9302, it cannot be ruled out that the observed efficacy *in vivo* may be due, in part, to combinatorial blockade of multiple ASCT2 substrates. Although we observed that glutamine withdrawal

or combinatorial ASCT2-substrate withdrawal had essentially indistinguishable effects on cell viability in V-9302-sensitive cancer cells, combinatorial depletion of ASCT2 substrates led to enhanced cell death in a portion of the cell lines evaluated. Collectively, these factors may, at least in part, explain the difference in efficacy between V-9302 and CB-839 observed in this study. The compound reported here also exhibits unique qualities that another reported inhibitor of glutamine uptake, GPNA, does not. Previously reported as an ASCT2 inhibitor, GPNA exhibits poor potency and selectivity in human cells<sup>14,35</sup>.

We identified several molecular determinants associated with response to V-9302; many of these affect facets of cancer cell growth and proliferation, cell death, and oxidative stress (Fig. 6b). In multiple models, V-9302 exposure resulted in decreased mTOR activity as assessed by p-S6 and p-Akt (Ser473) levels, which is consistent with diminished amino acid transport and metabolism<sup>18</sup>. Indeed, we found that mice treated chronically with V-9302 exhibited decreased plasma glutamine levels, which suggests, in part, diminished exchange via LAT1. In support of this, mTOR activity following V-9302 was decreased in all models evaluated. In spite of this, we observed elevated p-PRAS40 levels in V-9302-treated COLO 205 xenografts, suggesting prosurvival cap-dependent translation<sup>36</sup>. Although Akt is known to be a major regulator of PRAS40 phosphorylation, the data presented here point to Akt-independent PRAS40 regulation, perhaps through proto-oncogene PIM-1 (ref. 37). Interestingly, the observed increase in p-GSK-3 $\beta$  levels in COLO 205 xenografts following V-9302 treatment could also be explained by PIM-1 activity<sup>38</sup>, suggesting potential synergy between V-9302 and an inhibitor of the PIM-1 kinase. Data stemming from global metabolomic analysis were also consistent with impaired amino acid transport in V-9302-treated tumors, with a considerable impact on metabolites related to the ASCT2 substrates glutamine and serine. Given the anaplerotic nature of glutamine, it was not surprising that metabolites related to ATP production were diminished in V-9302-treated tumors. We consistently observed that V-9302 exposure led to diminished p-ERK levels in tumor cells *in vitro* and *in vivo*, which is potentially related to an extra-mitochondrial role for glutamine. Although V-9302 treatment did not fully abolish p-ERK levels, it was intriguing that V-9302-treated COLO 205 xenografts exhibited both decreased p-ERK and decreased BrdU incorporation, suggesting diminished proliferation. Indeed, prior studies have shown that glutamine can activate MAPK signaling independently of EGFR ligand activation<sup>39</sup>, suggesting that glutamine deprivation may exert antiproliferative effects, as shown here.

Elevated autophagy was another notable characteristic of the V-9302-mediated response *in vitro* and *in vivo*. Combining V-9302 with an autophagy inhibitor further decreased the viability of V-9302-sensitive cells, as elevated autophagy was likely a prosurvival response to substrate starvation; this potentially illuminates a future therapeutic strategy using combination treatment. In addition to autophagy, substantially elevated apoptosis was frequently observed in V-9302-treated tumors. Given that autophagy in this setting appeared to be protective, it is likely that the cell death response to V-9302 was mediated at least in part by apoptosis.

A third feature of the response to V-9302 was elevated oxidative stress. Frequently derived from glutamine, glutathione is a key modulator of oxidative stress. We observed that V-9302 impacted the redox state of glutathione in multiple models, leading to correspondingly increased levels of ROS. Additional markers elevated in V-9302-treated COLO 205 xenografts attributable to oxidative stress included elevated cleaved PARP, p38, and p53.

In summary, we report the first pharmacological inhibitor, to our knowledge, of the glutamine transporter ASCT2. These results not only illustrate the promising nature of the lead compound V-9302

but also support the concept that antagonizing glutamine metabolism at the transporter level represents a potentially viable approach in precision cancer medicine. Pairing patients harboring glutamine-dependent tumors with this new class of inhibitors will require validated biomarkers. As the expression of a transporter alone does not necessarily correlate with its activity, we were not surprised that the response to V-9302 did not correlate with levels of ASCT2 expression in tumors. Furthermore, larger studies are needed to evaluate correlates of V-9302 response and oncogene status. However, we did note that tumor cells sensitive to V-9302 were also sensitive to glutamine withdrawal as well as ASCT2 substrate withdrawal, suggesting that response to V-9302 is likely a function of transporter activity and a tumor's reliance upon that. Furthermore, considering that combining V-9302 with an inhibitor of autophagy resulted in a greater impact on cell viability, it cannot be ruled out that sensitivity to V-9302 may be predicated by a cancer cell's ability to use autophagy as a means to rescue the ASCT2-substrate-deprived phenotype. Importantly, the activity of ASCT2 can be quantitatively assessed using noninvasive PET imaging of glutamine uptake, which may represent a translational biomarker reflective of tumors likely to respond to V-9302 and similar agents.

## METHODS

Methods, including statements of data availability and any associated accession codes and references, are available in the [online version of the paper](#).

*Note: Any Supplementary Information and Source Data files are available in the online version of the paper.*

## ACKNOWLEDGMENTS

The authors acknowledge M. Tantawy for assistance with PET imaging, F. Revetta for histology expertise, and A. Rosenberg and A. Cohen for helpful discussions and editorial assistance. The authors wish to acknowledge research support from the Vanderbilt Ingram Cancer Center Support Grant (National Institutes of Health (NIH) National Cancer Institute (NCI) P30CA068485, H.C.M.), which supports the Vanderbilt-Ingram Cancer Center (VICC) Chemical Synthesis Core, Vanderbilt University Medical Center (VUMC) Radiochemistry Core, and Center for Small Animal Imaging; the Kleberg Foundation (H.C.M.); a Vanderbilt Trans-Institutional Program (TIPS) Award to the Vanderbilt Center for Molecular Probes (H.C.M.); the Vanderbilt Specialized Program of Research Excellence (SPORE) in Gastrointestinal Cancer (NIH NCI P50CA095103, R.J.C. and H.C.M.); an Outstanding Investigator Award from the NCI (R35CA197570, R.J.C.); and the Vanderbilt Digestive Disease Research Center (NIH National Institute of Diabetes and Digestive and Kidney Diseases (NIDDK) P30DK058404, H.C.M.).

## AUTHOR CONTRIBUTIONS

M.L.S. performed or designed most of the experiments with assistance from A.F., L.G., P.Z., and J.L. S.T.S. and J.A.S. performed computational modeling. J.K. and R.J.C. performed organoid studies. J.B. enrolled individuals who provided tissues for organoids and PDXs. J.T.S. and M.C.S. performed optical redox ratio measurements. M.O.J. and J.C.R. performed T cell experiments. M.K.W. interpreted pathology samples. M.L.N. oversaw radiopharmaceutical production and provided technical assistance. H.C.M. designed and supervised the study. M.L.S., M.L.N., and H.C.M. wrote the manuscript. All authors edited and approved the manuscript.

## COMPETING FINANCIAL INTERESTS

The authors declare no competing financial interests.

Reprints and permissions information is available online at <http://www.nature.com/reprints/index.html>. Publisher's note: Springer Nature remains neutral with regard to jurisdictional claims in published maps and institutional affiliations.

1. Pochini, L., Scalise, M., Galluccio, M. & Indiveri, C. Membrane transporters for the special amino acid glutamine: structure/function relationships and relevance to human health. *Front. Chem.* **2**, 61 (2014).



2. Jin, L., Alesi, G.N. & Kang, S. Glutaminolysis as a target for cancer therapy. *Oncogene* **35**, 3619–3625 (2016).
3. Hassanein, M. *et al.* SLC1A5 mediates glutamine transport required for lung cancer cell growth and survival. *Clin. Cancer Res.* **19**, 560–570 (2013).
4. van Geldermalsen, M. *et al.* ASCT2/SLC1A5 controls glutamine uptake and tumour growth in triple-negative basal-like breast cancer. *Oncogene* **35**, 3201–3208 (2016).
5. Schulte, M.L. *et al.* Non-invasive glutamine PET reflects pharmacological inhibition of BRAF<sup>V600E</sup> *in vivo*. *Mol. Imaging Biol.* **19**, 421–428 (2017).
6. Gao, P. *et al.* c-Myc suppression of miR-23a/b enhances mitochondrial glutaminase expression and glutamine metabolism. *Nature* **458**, 762–765 (2009).
7. Watanabe, T. *et al.* Differential gene expression signatures between colorectal cancers with and without KRAS mutations: crosstalk between the KRAS pathway and other signalling pathways. *Eur. J. Cancer* **47**, 1946–1954 (2011).
8. Romero, R. *et al.* *Keap1* loss promotes *Kras*-driven lung cancer and results in dependence on glutaminolysis. *Nat. Med.* **23**, 1362–1368 (2017).
9. Shukla, K. *et al.* Design, synthesis, and pharmacological evaluation of bis-2-(5-henylacetamido-1,2,4-thiadiazol-2-yl)ethyl sulfide 3 (BPTES) analogs as glutaminase inhibitors. *J. Med. Chem.* **55**, 10551–10563 (2012).
10. Harding, J.J. *et al.* Safety and tolerability of increasing doses of CB-839, a first-in-class, orally administered small molecule inhibitor of glutaminase, in solid tumors. *J. Clin. Oncol.* **33**, 2512 (2015).
11. Rhoads, J.M. *et al.* Glutamine metabolism stimulates intestinal cell MAPKs by a cAMP-inhibitable, Raf-independent mechanism. *Gastroenterology* **118**, 90–100 (2000).
12. Willems, L. *et al.* Inhibiting glutamine uptake represents an attractive new strategy for treating acute myeloid leukemia. *Blood* **122**, 3521–3532 (2013).
13. Schulte, M.L., Khodadadi, A.B., Cuthbertson, M.L., Smith, J.A. & Manning, H.C. 2-Amino-4-bis(aryloxybenzyl)aminobutanoic acids: a novel scaffold for inhibition of ASCT2-mediated glutamine transport. *Bioorg. Med. Chem. Lett.* **26**, 1044–1047 (2016).
14. Esslinger, C.S., Cybulski, K.A. & Rhoderick, J.F. *N<sub>r</sub>*-Aryl glutamine analogues as probes of the ASCT2 neutral amino acid transporter binding site. *Bioorg. Med. Chem.* **13**, 1111–1118 (2005).
15. Lomenick, B. *et al.* Target identification using drug affinity responsive target stability (DARTS). *Proc. Natl. Acad. Sci. USA* **106**, 21984–21989 (2009).
16. Canul-Tec, J.C. *et al.* Structure and allosteric inhibition of excitatory amino acid transporter 1. *Nature* **544**, 446–451 (2017).
17. Fuchs, B.C. & Bode, B.P. Amino acid transporters ASCT2 and LAT1 in cancer: partners in crime? *Semin. Cancer Biol.* **15**, 254–266 (2005).
18. Nicklin, P. *et al.* Bidirectional transport of amino acids regulates mTOR and autophagy. *Cell* **136**, 521–534 (2009).
19. Vichai, V. & Kirtikara, K. Sulforhodamine B colorimetric assay for cytotoxicity screening. *Nat. Protoc.* **1**, 1112–1116 (2006).
20. Rathmell, J.C. T cell Myc-tabolism. *Immunity* **35**, 845–846 (2011).
21. Skala, M. & Ramanujam, N. Multiphoton redox ratio imaging for metabolic monitoring *in vivo*. *Methods Mol. Biol.* **594**, 155–162 (2010).
22. Walsh, A.J. *et al.* Quantitative optical imaging of primary tumor organoid metabolism predicts drug response in breast cancer. *Cancer Res.* **74**, 5184–5194 (2014).
23. DeBerardinis, R.J., Sayed, N., Ditsworth, D. & Thompson, C.B. Brick by brick: metabolism and tumor cell growth. *Curr. Opin. Genet. Dev.* **18**, 54–61 (2008).
24. Hanover, J.A., Krause, M.W. & Love, D.C. The hexosamine signaling pathway: O-GlcNAc cycling in feast or famine. *Biochim. Biophys. Acta* **1800**, 80–95 (2010).
25. Obeid, L.M., Linardic, C.M., Karolak, L.A. & Hannun, Y.A. Programmed cell death induced by ceramide. *Science* **259**, 1769–1771 (1993).
26. Tresse, E., Kosta, A., Giusti, C., Luciani, M.F. & Golstein, P. A UDP-glucose derivative is required for vacuolar autophagic cell death. *Autophagy* **4**, 680–691 (2008).
27. Sentelle, R.D. *et al.* Ceramide targets autophagosomes to mitochondria and induces lethal mitophagy. *Nat. Chem. Biol.* **8**, 831–838 (2012).
28. Dall'Armi, C., Devereaux, K.A. & Di Paolo, G. The role of lipids in the control of autophagy. *Curr. Biol.* **23**, R33–R45 (2013).
29. Shatz, O., Holland, P., Elazar, Z. & Simonsen, A. Complex relations between phospholipids, autophagy, and neutral lipids. *Trends Biochem. Sci.* **41**, 907–923 (2016).
30. Huang, F., Zhang, Q., Ma, H., Lv, Q. & Zhang, T. Expression of glutaminase is upregulated in colorectal cancer and of clinical significance. *Int. J. Clin. Exp. Pathol.* **7**, 1093–1100 (2014).
31. Xiang, Y. *et al.* Targeted inhibition of tumor-specific glutaminase diminishes cell-autonomous tumorigenesis. *J. Clin. Invest.* **125**, 2293–2306 (2015).
32. Seltzer, M.J. *et al.* Inhibition of glutaminase preferentially slows growth of glioma cells with mutant IDH1. *Cancer Res.* **70**, 8981–8987 (2010).
33. Gross, M.I. *et al.* Antitumor activity of the glutaminase inhibitor CB-839 in triple-negative breast cancer. *Mol. Cancer Ther.* **13**, 890–901 (2014).
34. Suzuki, S. *et al.* Phosphate-activated glutaminase (GLS2), a p53-inducible regulator of glutamine metabolism and reactive oxygen species. *Proc. Natl. Acad. Sci. USA* **107**, 7461–7466 (2010).
35. Chiu, M. *et al.* GPNA inhibits the sodium-independent transport system L for neutral amino acids. *Amino Acids* **49**, 1365–1372 (2017).
36. McKinley, E.T., Zhao, P., Coffey, R.J., Washington, M.K. & Manning, H.C. 3'-Deoxy-3'-[<sup>18</sup>F]-fluorothymidine PET imaging reflects PI3K–mTOR-mediated pro-survival response to targeted therapy in colorectal cancer. *PLoS One* **9**, e108193 (2014).
37. Wiza, C., Nascimento, E.B. & Ouwens, D.M. Role of PRAS40 in Akt and mTOR signaling in health and disease. *Am. J. Physiol. Endocrinol. Metab.* **302**, E1453–E1460 (2012).
38. Santio, N.M. *et al.* The PIM1 kinase promotes prostate cancer cell migration and adhesion via multiple signalling pathways. *Exp. Cell Res.* **342**, 113–124 (2016).
39. Rhoads, J.M. *et al.* L-Glutamine stimulates intestinal cell proliferation and activates mitogen-activated protein kinases. *Am. J. Physiol.* **272**, G943–G953 (1997).

## ONLINE METHODS

**General methods and reagents and supplies.** All reagents and supplies were obtained from commercial suppliers and in some cases were further purified on an as-needed basis. Analytical thin-layer chromatography (TLC) was performed on silica gel plates from Sorbent Technologies with direct visualization via ultraviolet (UV) light and/or the use of ninhydrin or potassium permanganate staining. Chromatographic purification of intermediates was performed using silica or RediSep Rf C18 flash columns on a CombiFlash Rf automated chromatography system. All  $^1\text{H}$  and  $^{13}\text{C}$  nuclear magnetic resonance (NMR) spectra were recorded on a Bruker AV400 (400 MHz and 100 MHz, respectively). All  $^1\text{H}$  and  $^{13}\text{C}$  chemical shifts are reported in parts per million (p.p.m.) relative to residual solvent peaks. CB-839 was obtained from Calithera Biosciences. Immortalized cell lines were purchased from commercial vendors (ATCC) and were authenticated using a commercial vendor (Genetica). Mice were purchased from Envigo and used in accordance with Institutional and Federal guidelines. All animal procedures were approved by the Vanderbilt University Institutional Animal Care and Use Committee (IACUC). Human CRC organoids were obtained from subjects enrolled in a clinical trial at Vanderbilt University Medical Center in accordance with an Institutional Review Board (IRB)-approved protocol. For all statistical comparisons, the variance between groups being compared was similar.

**Synthesis of V-9302.** V-9302 was prepared as previously described<sup>13</sup>. For this study, V-9302 was purified by reverse phase (C18) column chromatography (10–90% acetonitrile in water gradient over 60 min), giving a final yield of up to 72% over two steps.  $^1\text{H}$  NMR (400 MHz,  $\text{CDCl}_3$ )  $\delta$  (ppm): 7.23 (d,  $J = 7.36$  Hz, 2H), 7.20–7.15 (m, 4H), 7.10–7.06 (m, 6H), 6.89–6.82 (m, 2H), 5.06–4.97 (m, 4H), 3.81 (d,  $J = 12.92$  Hz, 2H), 3.64 (d,  $J = 12.88$  Hz, 2H), 3.00 (dd,  $J = 7.38$  Hz, 4.90 Hz, 1H), 2.75 (s, 2H), 2.29 (s, 6H), 2.01–1.90 (m, 1H), 1.90–1.77 (m, 1H).  $^{13}\text{C}$  NMR (100 MHz,  $\text{CDCl}_3$ )  $\delta$  (ppm): 172.66, 156.91, 138.04, 136.86, 131.82, 129.14, 128.53, 128.42, 128.15, 124.53, 120.91, 112.38, 70.07, 55.75, 52.70, 52.11, 26.51, 21.34. Positive electrospray ionization time-of-flight (TOF ES+) high-resolution mass spectrometry (HRMS),  $\text{C}_{34}\text{H}_{38}\text{N}_2\text{O}_4$ ,  $[\text{M} + \text{H}]^+$ : calculated mass, 539.2904 m/z; found mass, 539.2891 m/z.

**General procedure for  $^3\text{H}$ -labeled amino acid uptake assays.** Live-cell amino acid uptake assays using HEK-293 cells were carried out in 96-well plates (CulturPlate-96, Perkin Elmer). 96-well plates were coated with poly-D-lysine before the assay. Cells were plated at a density of 35,000 cells per well 24 h before carrying out the assay. Each set of conditions was replicated at least three times, technically and biologically (three experiments performed in triplicate). Cells were washed three times with 100  $\mu\text{l}$  of assay buffer (containing 137 mM NaCl, 5.1 mM KCl, 0.77 mM  $\text{KH}_2\text{PO}_4$ , 0.71 mM  $\text{MgSO}_4 \cdot 7\text{H}_2\text{O}$ , 1.1 mM  $\text{CaCl}_2$ , 10 mM D-glucose, and 10 mM HEPES) to remove cell media.  $^3\text{H}$  amino acid (500 nM) in the same buffer was added concomitantly with V-9302 and allowed to incubate for 15 min at 37 °C. For ASCT2-mediated  $^3\text{H}$  glutamine uptake assays, 5 mM of the system L inhibitor 2-amino-2-norbornanecarboxylic acid (BCH) was added and the assay buffer was adjusted to pH 6.0. For selectivity studies, no BCH was added and the assay was conducted at pH 7.4. Following the incubation period, the  $^3\text{H}$  glutamine and inhibitor were removed, and cells were washed three times with assay buffer. The cells were then lysed through the addition of 50  $\mu\text{l}$  1 M NaOH. For reading, 150  $\mu\text{l}$  of scintillation fluid (Microscint 40, Perkin Elmer) was added, and the plates were counted on a scintillation counter (Topcount, Perkin Elmer).  $\text{IC}_{50}$  values were calculated using GraphPad Prism version 6 for Mac OS X (GraphPad Software, San Diego, CA USA; <http://www.graphpad.com/>). Error is reported as s.d.

**Procedure for *in silico* docking studies of V-9302.** A model of an inhibitor-bound conformation of hASCT2 was used as a target for ligand docking of V-9302. 2D structures for all ligands were generated in ChemDraw, imported into Tripos Sybyl for conversion into 3D structures using CONCORD, and docked using RosettaLigand<sup>40</sup>. Figures for docked complexes were generated and ray-traced using PyMOL (The PyMOL Molecular Graphics System, Version 1.5.0.4, Schrodinger, LLC). In addition, fragment constraints were used to encourage placement of the amino acid analog main-chain atoms in a location analogous to the positions that were experimentally determined for (2S, 3S)-3-[3-(4-

(trifluoromethyl)benzoylamino]-benzyloxy]aspartate (TFB-TBOA) in its co-crystal structure within the homologous human excitatory amino acid transporter 1 (hEAAT1; Protein Data Bank (PDB) ID: 5MJU) protein<sup>16</sup>. Seeding the docking calculations in this way yielded better-scoring docking poses using the empirically derived scoring function, suggesting that this feature of the binding interaction may be conserved between these two systems.

For comparative studies of ASCT2 and LAT1, predictive structures used for docking were generated using homology modeling. To determine suitable template structures, the primary sequence of ASCT2 was extracted from gene *SLC1A5* (UniProt Knowledgebase (UniProtKB) ID: Q15758). Using the PDB Search tool within MOE (version 2014.09, Chemical Computing Group), ASCT2 alignments were generated with the crystal structure of hEAAT1. The primary sequence of LAT1 used to determine predictive structures was extracted from gene *SLC7A5* (UniProtKB ID: Q01650). LAT1 homology model structures were generated from crystal structures of the  $\text{Arg}^+$ -bound conformation of *Escherichia coli* AdiC and the ApcT transporter derived from *Methanocaldococcus jannaschii* (PDB IDs: 3L1L and 3GIA, respectively). MOE's homology model application generated initial structures with a well-conserved binding pocket using the templates and respective sequence alignments. All resulting ASCT2 and LAT1 structures underwent energy minimization using Amber12 force field potentials and protonation. In order to mimic the lipid bilayer environments of ASCT2 and LAT1, homology models were embedded and relaxed into the membrane using the RosettaMP framework. Upon further refinement, top scoring models of both ASCT2 and LAT1 were used for docking simulations of V-9302 and additional ligands according to the RosettaLigand protocol. Ligand rotational conformer libraries were generated using energy minimization in MMFF94x force field potentials and then screened using the MOE conformer search tool. The binding site was identified using prior knowledge of homology binding sites and Surflex-Dock results. Each simulation consisted of 500 iterations while scoring the protein–ligand interface energies. Final models were sorted based on interface\_delta\_X scores, and evidence regarding steric hindrance penalties was extracted on the basis of if\_X\_fa\_rep energies.

***In silico* alanine scan.** Docking studies were performed to place V-9302 into the amino acid-binding site of an ASCT2 homology model. The highest scoring poses were found when the constraints were enabled to favor poses that anchored the amino acid moiety of the ligands to a similar binding orientation as TFB-TBOA in the structure of the homologous protein hEAAT1. *In silico* mutagenesis experiments were conducted by individually changing side chains to alanine without otherwise changing the conformation of the protein or ligand in Rosetta. RosettaLigand was then used to rescore the same V-9302 docking pose with each of these Ala mutants. The docking score for each mutant was then compared with the score for the WT model to assess the WT side chain contribution to the overall score in this binding pose.

**Generation of HEK-293 cells with tetracycline-inducible ASCT2 expression.** T-REX-293 cells (Invitrogen R71007) were transfected with the plasmid pCDNA5-TO-h-SLC1A5 (Invitrogen V1033-20) according to the manufacturer's protocol. The cloning sites consisted of Not1 and XbaI sites; insert OriGene SC116600. Stably transfected clones were selected via hygromycin (150  $\mu\text{g}/\text{ml}$ ).

**Drug affinity responsive target stability assay.** DARTS was carried out as previously described<sup>15</sup> using T-REX-293 cells with tetracycline-inducible expression of ASCT2 or lysate from 115 mg of homogenized mouse brain for ASCT1. Lysates were exposed to V-9302 at varying concentrations for 35–45 min at room temperature with shaking. Lysates were then incubated at room temperature with the protease Thermolysin (1:100 and 1:200 total enzyme to total substrate) for 30 min. ASCT2 was measured by immunoblotting (ASCT2 antibody: Millipore ABN73; ASCT1 antibody: Cell Signaling 8442).

**shRNA.** HCC1806 cells were transfected with a lentiviral vector (pLKO.1) containing control shRNA (Sigma SHC002V) or shRNA against ASCT2 (Sigma SHCLNV-NM\_005628): 5'-CCGGCTGGATTATGAGGAATGGATACTCGA GTATCCATTCTCATAATCCAGTTTGTG-3'. ASCT2 expression was measured by immunoblotting (ASCT2 antibody: Millipore ABN73) at 72 h post transduction and after puromycin selection.

**Cell viability screens.** Viability was evaluated using commercially available chemiluminescent reagents (CellTiter-Glo, Promega Corp. G7572; MultiTox Glo, Promega Corp. G9270) in 96-well-plate format according to the manufacturer's protocols. Cells were exposed to vehicle, V-9302, CB-839, V-9302 + chloroquine (CLQ), or CB-839 + CLQ and incubated for a period of 48 h. Subsequently, CellTiter-Glo reagent was added, and the plates were read using a plate reader (BioTek Synergy 4) with standard settings. Each set of conditions was replicated at least three times, technically and biologically. Error is reported as s.d. The sulforhodamine B assay was run analogously to the above assays as previously described<sup>19</sup>.

**Measurement of glutathione and reactive oxygen species.** Glutathione levels were measured using a commercially available kit (Cayman Chemical 703002) according to the manufacturer's protocol. ROS were concurrently measured in cells using CM-H2DCFDA (Life Technologies C6827) coupled with flow cytometry in accordance with the manufacturer's protocol. The assay was replicated at least three times, technically and biologically. Significance was calculated using a *t*-test in GraphPad Prism. Error is reported as s.d.

**Measurement of p-ERK.** Detection of activated ERK in cell lysates was enabled by the AlphaScreen SureFire ERK assay (Perkin Elmer) performed according to the manufacturer's protocol. Cells were plated in 96-well plates for 24 h before the assay. Cells were treated with either vehicle or the indicated concentrations of V-9302 or CB-839 for 48 h (Supplementary Fig. 9).

**Measurement of autophagic flux.** Autophagic flux was measured using the CYTO-ID autophagy detection kit (Enzo Life Sciences ENZ-51031). HCC1806 and HT29 cells were seeded in 96-well plates the day before the experiment. After overnight incubation, cells were treated with V-9302, CB-839, and 500 nM rapamycin as a positive control or the combinations thereof with 10  $\mu$ M CLQ for 18 h. Following treatment, cells were gently washed with assay buffer followed by addition of the dual-color detection solution and incubation at 37 °C for 30 min. The plate was analyzed on a fluorescence microplate reader (BioTek Synergy 4).

**Immunoassays.** For immunoreactivity studies, tissue samples were diluted to 100 mg/ml in lysis buffer (Cell Signaling Technology 7018s) and subsequently homogenized, sonicated, and spun at 3,500 r.p.m. for 1 min. Lysate samples were then screened against an array of target-specific capture antibodies using PathScan Intracellular Signaling Array Kits (Cell Signaling Technology 7323) in accordance with the manufacturer's instructions and were developed using HyBlot CL autoradiography film (Denville Scientific, Inc., e3012). Processed films were digitized using an Epson Perfection V600 Photo scanner, and the relative pixel intensities for each blot were quantified using the image processing software ImageJ. Complementary western blot studies were performed through loading 20–40  $\mu$ g of protein into 7.5–12% SDS-PAGE gels, which were transferred to PVDF membranes (Perkin Elmer) and resolved using electrophoresis. Membranes were blocked overnight at 4 °C in Tris-buffered saline with 0.1% Tween-20 (TBST) containing 5% nonfat dry milk powder and were subsequently incubated with antibodies against p-ERK1 (Thr202) and p-ERK2 (Tyr204) (Cell Signaling 4370), p-S6 (Cell Signaling 4858), LC3B (anti-LC3B, Cell Signaling 2775), or  $\beta$ -tubulin (Novus Biologicals NB600-936). Membrane chemiluminescence was visualized on a Xenogen IVIS 200 system.

**Immunofluorescence.** HCC1806 cells were treated with V-9302 (25  $\mu$ M aqueous, 1% DMSO) for 48 h. Following treatment, cells were fixed with 70% methanol for 5–10 min. LC3B was visualized with 1:100 primary antibody (anti-LC3B, Cell Signaling 2775) at 37 °C for 45 min followed by application of 1:600 secondary antibody (Rhodamine Red, Invitrogen R6394) at 37 °C for 30 min and DAPI for 4 min. Images were acquired with a fluorescence microscope and were visualized at 40 $\times$  magnification.

**In vivo BrdU incorporation assay.** Four hours after the final treatment, mice were injected with BrdU labeling reagent (Zymed Laboratories, South San Francisco, CA). Six hours after injection, the mice were killed. Mouse tumors

were harvested, fixed in paraffin, and sectioned. Slides were stained with anti-BrdU primary antibody (mouse IgG; Life Technologies 03-3900) followed by Rhodamine Red-labeled goat anti-mouse secondary antibody (ThermoFisher R-6393, Invitrogen Molecular Probes, Carlsbad, CA). Sections were counterstained with the nucleic acid dye DAPI. Photographs were taken, scanned into Photoshop software, and quantified. The mean and standard error of BrdU-incorporating cells were determined (*n* = 3). To quantify endothelial cell proliferation *in vivo*, high-power photographs were taken. The endothelial cells surrounding blood vessels were confirmed by two separate observers and quantified for each treatment condition as stated above (*n* = 6).

**Immunohistochemistry.** For immunohistochemistry, mice were euthanized, and tumor tissue samples were collected within 4 h of the final V-9302 dose, fixed in 10% formalin for 24 h, and then stored in 70% ethanol in PBS. Tissues were sectioned (5- $\mu$ m thickness) and stained for p-S6 (Cell Signaling 4858) and caspase 3 (Cell Signaling 9661). Tissue slides were imaged at 20 $\times$  magnification.

**Fluorescence redox ratio imaging.** HCC 1806 cells were plated on 35-mm glass-bottom petri dishes for imaging (MatTek Corp). Fluorescence intensity and lifetime images were acquired using a custom-built multiphoton fluorescence lifetime system (Bruker), with a 40 $\times$  oil-immersion objective (1.3 NA) and an inverted microscope (TiE, Nikon). A titanium:sapphire laser (Chameleon Ultra II, Coherent) was tuned to 750 nm for two-photon excitation of NAD(P)H and tuned to 890 nm for two-photon excitation of FAD. A 440/80-nm bandpass filter was used to collect NAD(P)H fluorescence emission, and a 550/100-nm bandpass filter was used to collect FAD emission. A pixel dwell time of 4.8  $\mu$ s was used to collect images that were 256 pixels  $\times$  256 pixels, with a total integration time of 60 s. A GaAsP photomultiplier (PMT; H7422P-40, Hamamatsu) detected emitted photons. The field of view acquired was 270  $\mu$ m  $\times$  270  $\mu$ m, and six fields of view were acquired per treatment group. Time-correlated single-photon counting electronics (SPC-150, Becker & Hickl) were used to acquire fluorescence decay curves. The second harmonic-generated signal from urea crystals at 900-nm excitation was used to measure the instrument response function, which was found to have a full width at a half maximum of 220 ps. Fluorescence lifetime validation was performed through imaging a fluorescent bead (Polysciences, Inc.) and confirming that the measured lifetime (2.1 ns) agreed with previously published values<sup>22</sup>. The assay was replicated at least three times with technical and biological replicates.

A histogram of photon counts per temporal bin (decay curve) was constructed for each pixel in the image and then deconvolved with the instrument response function. Decay curves were then fit to a two-component exponential decay to account for the distinct free and protein-bound lifetimes of NAD(P)H and FAD using SPCImage software (Becker & Hickl). The decay fit is given by equation (1), where  $I(t)$  represents the fluorescence intensity measured at time  $t$  after the laser pulse;  $\alpha_1$  and  $\alpha_2$  represent the fractional contributions of the short and long lifetime components to the overall intensity, respectively;  $T_1$  and  $T_2$  represent the fluorescence lifetimes of the short and long lifetime components, respectively; and  $C$  represents a constant level of background light.

$$I(t) = \alpha_1 e^{-t/T_1} + \alpha_2 e^{-t/T_2} + C \quad (1)$$

The mean lifetime ( $T_m$ ) of NAD(P)H or FAD represents the weighted average of the short and long lifetime components (Equation (2)).

$$T_m = \alpha_1 \times T_1 + \alpha_2 \times T_2 \quad (2)$$

An automated cell segmentation routine was written using CellProfiler to identify individual cell cytoplasm and extract average fluorescence intensity and fluorescence lifetime values for each cell in the field of view. Intensity values for each pixel were calculated through integrating the decay curve for each pixel. Optical redox ratio values were calculated for each cell by dividing the average intensity of NAD(P)H by the average intensity of FAD. Optical redox ratio values were normalized to vehicle. For each imaging endpoint, values for all cells imaged in each treatment group were averaged together to generate mean and standard error values. An unpaired *t*-test with Welch's correction was performed for all comparisons of imaging values.



**Organoid culture and viability assay.** Human CRC-derived organoids were prepared following a previously reported method with modification<sup>41</sup>. Briefly, specimens from freshly resected tumors were minced and digested with 2 mg/ml type 2 collagenase (Worthington, NJ, USA). Samples were passed through 40- $\mu$ m filters (Greiner Bio One, NC, USA), and epithelial cells trapped on the filters were embed in Matrigel (Corning, MA, USA) and cultured with advanced DMEM/F-12 supplemented with N2 and B27 supplements (Thermo Fisher, MA, USA), 50 ng/ml recombinant human epidermal growth factor (rhEGF; R&D Systems, MN, USA), and 1% Antibiotic-Antimycotic (Corning). For the viability assay, organoids were dissociated by TrypLE express (Thermo Fisher) and suspended in Matrigel. 5  $\mu$ l of cell suspension in Matrigel drops was placed into untreated 96-well plates (Corning) and overlaid with experimental medium, which consisted of V-9302, CB-839, or vehicle at the indicated concentration (**Fig. 4g** and **Supplementary Fig. 14**) in advanced DMEM/F12 supplemented with N2 and B27 supplements, 1% Antibiotic-Antimycotic, and 4 mM L-glutamine (GE Healthcare, OH, USA). After 4 d of culture, images of the organoids in Matrigel were captured and the number of viable cells was quantified with CellTiter Aqueous One Cell Proliferation Assay kit (Promega, WI, USA) and a Synergy 4 plate reader (BioTek, VT, USA). The assay was replicated at least three times with technical and biological replicates. Significance was calculated using a *t*-test in GraphPad Prism. Error is reported as s.d.

**V-9302 plasma stability assay.** Whole-blood samples ( $n = 5$  mice) were assayed for V-9302 levels with respect to time by Sano Informed Prescribing, Inc. (Franklin, TN). Liquid chromatography–tandem mass spectroscopy (LC–MS/MS) analyses were performed via reverse-phase chromatography using a Shimadzu Nexera X2 UPLC (Columbia, MD) coupled with a QTrap 5500 (Sciex, Framingham, MA, USA). A standard curve and quality-control samples were made by spiking V-9302 into fresh whole blood and then applying this to 10  $\mu$ l Mitra Microsamplers (Neoteryx, LLC, Torrance, CA). Blank samples were made using fresh whole blood applied to Mitra Microsamplers and were allowed to dry for at least 24 h. All data were collected using Sciex Analyst 1.6.2 software and analyzed with MultiQuant 3.0 software. Error is reported as s.d.

**Plasma metabolite analysis.** To quantify plasma glutamine and glucose, whole blood was collected from healthy mice ( $n = 10$ ) chronically exposed to V-9302 (75 mg per kg body weight, daily) or vehicle. Mice were euthanized 4 h after the final treatment. Following centrifugation, plasma was collected and 50  $\mu$ l was added to a 96-well plate in triplicate. Plasma samples were diluted with 50  $\mu$ l of assay buffer (YSI 2357), and glucose and glutamine were quantified directly using a YSI 2950D Biochemistry Analyzer (YSI, Inc.). Significance was calculated using a *t*-test in GraphPad Prism. Error is reported as s.d.

**CD8<sup>+</sup> cell studies.** CD8<sup>+</sup> cells were isolated from spleens of 8- to 12-week-old C57BL/6 mice on standard chow from Jackson Labs maintained under Vanderbilt University Institutional Animal Care and Use Committee (IACUC)-approved protocols. CD8<sup>+</sup> cells were stained using the proliferative dye Cell Trace Violet (LifeTech) before stimulation per the manufacturer's protocol. Cells were stimulated on 5  $\mu$ g/ml anti-CD3- and anti-CD28-coated plates in medium containing IL-2 ('activated', 10 ng/ml) or on tissue-culture-treated plates in medium containing IL-7 ('naive', 1 ng/ml) for up to 7 d. Cells were removed daily, and their viability, cell counts, proliferation, and surface markers of activation were described. The cell-surface markers used were CD62L-FITC and APC, CD44-PE/Cy5, and CD25-PE. All data were acquired in triplicate on a MacsQuant Analyzer (Miltenyi Biotec) and analyzed using FlowJo version 10 (TreeStar software).

**Synthesis of [4-<sup>18</sup>F]fluoroglutamine.** [4-<sup>18</sup>F]fluoroglutamine and the requisite tosylate precursor were produced as previously reported<sup>5</sup>.

**Positron emission tomography imaging and analysis.** Mouse handling methods for PET imaging studies were as previously reported<sup>5,42</sup>. Prior to imaging, mice were allowed to acclimate to the facility environment for at least 1 h in a warmed chamber at 31.5 °C. Mice were administered 10.4–11.8 MBq

[4-<sup>18</sup>F]fluoroglutamine via intravenous injection and imaged using a Concorde Microsystems Focus 220 microPET scanner (Siemens Preclinical Solutions). During imaging, mice were maintained under 2% isoflurane anesthesia in oxygen at 2 liters/min and were kept warm for the duration of the PET scan. PET images in xenograft-bearing mice were acquired as 60-min dynamic data sets. Imaging was initiated 3 h post treatment with vehicle or V-9302 (75 mg per kg body weight). PET data were reconstructed using a 3D ordered subset expectation maximization/maximum a posteriori (OSEM3D/MAP) algorithm. The resulting 3D reconstructions had an  $x$ - $y$  voxel size of 0.474 mm and an interslice distance of 0.796 mm. ASIPro software (Siemens Preclinical Solutions) was used to manually draw 3D regions of interest surrounding the entire tumor volume. [4-<sup>18</sup>F]fluoroglutamine uptake was quantified as the percentage of the injected dose per gram of tissue (% ID/g). Significance was calculated using a *t*-test in GraphPad Prism. Error is reported as s.d.

**In vivo tumor studies.** For *in vivo* studies, cell line xenograft tumors were propagated in 6-week-old female athymic nude mice from immortalized cell lines. HCC-1806 ( $10 \times 10^6$  cells), HCT-116 ( $5 \times 10^6$ ), and HT29 ( $10 \times 10^6$ ) cells were injected. Palpable tumors were typically visible within 2–3 weeks. For imaging studies (HCC-1806), tumors were propagated to approximately 500 mm<sup>3</sup>. For treatment studies (HCT-116, HT29), tumors were propagated to approximately 200 mm<sup>3</sup> before therapy and were randomly assigned to treated and untreated cohorts. For generating the PDX, primary tumor tissue was obtained from a patient at Vanderbilt University Medical Center under a protocol approved by the Vanderbilt University Medical Center (VUMC)'s Institutional Review Board (IRB) and the Vanderbilt-Ingram Cancer Center (VICC) Scientific Review Committee. Written informed consent was obtained from all patients prior to tissue collection. The tumor tissue was genotyped within the VANTAGE core facility. The xenograft was generated as previously described<sup>41</sup>. Briefly, tumor tissues were sectioned into approximately 125-mm<sup>3</sup> pieces and then implanted subcutaneously without further manipulation. PDX tumors were propagated to the F<sub>3</sub> generation for V-9302 treatment studies. For treatment, V-9302 was reconstituted in a vehicle of PBS supplemented with 2% DMSO and administered intraperitoneally. Tumor volumes were measured manually using calipers every third day and were quantified using the formula  $V = W \times L \times (H/2)$ .

**Metabolomics.** HT-29 ( $n = 10$ ) tumor samples were harvested and snap frozen within 4 h of the final dose of V-9302 or vehicle. Metabolomic data acquisition was outsourced to Metabolon, Inc. Samples were prepared using the automated MicroLab STAR system from Hamilton Company. To remove protein, dissociate small molecules bound to protein or trapped in the precipitated protein matrix, and recover chemically diverse metabolites, proteins were precipitated with methanol under vigorous shaking for 2 min (Glen Mills GenoGrinder 2000), which was followed by centrifugation. The resulting extract was divided into five fractions: two for analysis using two separate reverse-phase ultra-performance liquid chromatography–tandem mass spectrometry (RP/UPLC–MS/MS) methods with positive-ion mode electrospray ionization (ESI), one for analysis by RP/UPLC–MS/MS with negative-ion mode ESI, one for analysis by hydrophilic interaction chromatography (HILIC)/UPLC–MS/MS with negative-ion mode ESI, and one sample that was reserved for backup. Samples were placed briefly on a TurboVap (Zymark) to remove the organic solvent. All procedures used a Waters ACQUITY UPLC and a Thermo Scientific Q-Exactiva high-resolution/accurate mass spectrometer interfaced with a heated electrospray ionization (HESI-II) source and an Orbitrap mass analyzer operated at 35,000 mass resolution. The sample extract was dried and then reconstituted in solvents compatible with each of the four methods. Each reconstituted solvent contained a series of standards at fixed concentrations to ensure injection and chromatographic consistency. One aliquot was analyzed using acidic positive-ion conditions that were chromatographically optimized for more hydrophilic compounds. In this method, the extract was gradient eluted from a C18 column (Waters UPLC BEH C18, 2.1 mm  $\times$  100 mm, 1.7  $\mu$ m) containing 0.05% perfluoropentanoic acid (PFPA) and 0.1% formic acid (FA) using water and methanol. Another aliquot was also analyzed using acidic positive-ion conditions; however, it was chromatographically optimized for more hydrophobic compounds. In this method, the extract was gradient eluted from the same aforementioned C18 column using methanol, acetonitrile, water, 0.05% PFPA, and 0.01% FA and was operated at

an overall higher organic content. Another aliquot was analyzed using basic negative-ion-optimized conditions using a separate dedicated C18 column. The basic extracts were gradient eluted from the column using methanol and water with 6.5 mM ammonium bicarbonate at pH 8. The fourth aliquot was analyzed via negative ionization following elution from a HILIC column (Waters UPLC BEH Amide, 2.1 mm × 150 mm, 1.7 μm) using a gradient consisting of water and acetonitrile with 10 mM ammonium formate, pH 10.8. Raw data were extracted, peak-identified, and quality-control processed using Metabolon's hardware and software. Compounds were identified through comparison with library entries of purified standards or recurrent unknown entities. Metabolon maintains a library based on authenticated standards that contains the retention time/index (RI), mass to charge ratio ( $m/z$ ), and chromatographic data (including MS/MS spectral data) for all molecules present in the library. Furthermore, biochemical identifications were based on three criteria: retention index within a narrow RI window of the proposed identification, accurate mass match to that in the library ± 10 p.p.m., and the MS/MS forward and reverse scores matched between the experimental data and authentic standards. The MS/MS scores are based on a comparison of the ions present in the experimental spectrum to the ions present in the library spectrum. Peaks were quantified using area under the curve. For studies spanning multiple days, a data normalization step was performed to correct for variation resulting from instrument interday tuning differences. For many studies, two types of statistical analysis were performed: significance tests and classification analysis. Standard statistical analyses were performed in

ArrayStudio on log-transformed data. For those analyses that were not standard in ArrayStudio, R (<http://cran.r-project.org/>) or JMP was used.

**Statistics and reproducibility.** Sample sizes and statistical tests for each experiment are denoted in the figure legends or the respective methods section. All analyses and graphs were generated with GraphPad Prism 6.  $P < 0.05$  was considered significant; exact  $P$  values can be found in the figures.

**Life Sciences Reporting Summary.** Further information on experimental design is available in the **Life Sciences Reporting Summary**.

**Data availability.** All data supporting the findings of this study are available from the corresponding author upon request. **Supplementary Data 1** contains complete metabolic data for V-9302.

40. Meiler, J. & Baker, D. ROSETTALIGAND: protein–small molecule docking with full side-chain flexibility. *Proteins* **65**, 538–548 (2006).
41. Kondo, J. *et al.* Retaining cell–cell contact enables preparation and culture of spheroids composed of pure primary cancer cells from colorectal cancer. *Proc. Natl. Acad. Sci. USA* **108**, 6235–6240 (2011).
42. McKinley, E.T. *et al.*  $^{18}$ F-DG-PET predicts pharmacodynamic response to OSI-906, a dual IGF-1R/IR inhibitor, in preclinical mouse models of lung cancer. *Clin. Cancer Res.* **17**, 3332–3340 (2011).

## Life Sciences Reporting Summary

Nature Research wishes to improve the reproducibility of the work that we publish. This form is intended for publication with all accepted life science papers and provides structure for consistency and transparency in reporting. Every life science submission will use this form; some list items might not apply to an individual manuscript, but all fields must be completed for clarity.

For further information on the points included in this form, see [Reporting Life Sciences Research](#). For further information on Nature Research policies, including our [data availability policy](#), see [Authors & Referees](#) and the [Editorial Policy Checklist](#).

### ▶ Experimental design

#### 1. Sample size

Describe how sample size was determined.

Sample size was chosen based on prior studies in our lab and by others in the literature. Power analyses were conducted where appropriate. All results are reported as a minimum of 3 independent experiments conducted in triplicate.

#### 2. Data exclusions

Describe any data exclusions.

No data were excluded from the manuscript

#### 3. Replication

Describe whether the experimental findings were reliably reproduced.

For each experiment, the results were reliably reproduced and all experiments are reported in the manuscript

#### 4. Randomization

Describe how samples/organisms/participants were allocated into experimental groups.

For all animal experiments, the animals were allocated into experimental groups such that the distribution of initial tumor volumes were roughly equal.

#### 5. Blinding

Describe whether the investigators were blinded to group allocation during data collection and/or analysis.

Investigators were not blinded to the group allocation during data collection. This was not possible as the investigators were also conducting the experiments and had to be aware of treated vs non-treated groups.

Note: all studies involving animals and/or human research participants must disclose whether blinding and randomization were used.

#### 6. Statistical parameters

For all figures and tables that use statistical methods, confirm that the following items are present in relevant figure legends (or in the Methods section if additional space is needed).

- |                                     |  |
|-------------------------------------|--|
| n/a                                 | Confirmed  |
| <input type="checkbox"/>            | <input checked="" type="checkbox"/> The <u>exact sample size</u> ( $n$ ) for each experimental group/condition, given as a discrete number and unit of measurement (animals, litters, cultures, etc.)                                    |
| <input type="checkbox"/>            | <input checked="" type="checkbox"/> A description of how samples were collected, noting whether measurements were taken from distinct samples or whether the same sample was measured repeatedly   |
| <input type="checkbox"/>            | <input checked="" type="checkbox"/> A statement indicating how many times each experiment was replicated   |
| <input type="checkbox"/>            | <input checked="" type="checkbox"/> The statistical test(s) used and whether they are one- or two-sided (note: only common tests should be described solely by name; more complex techniques should be described in the Methods section) |
| <input checked="" type="checkbox"/> | <input type="checkbox"/> A description of any assumptions or corrections, such as an adjustment for multiple comparisons   |
| <input type="checkbox"/>            | <input checked="" type="checkbox"/> The test results (e.g. $P$ values) given as exact values whenever possible and with confidence intervals noted   |
| <input type="checkbox"/>            | <input checked="" type="checkbox"/> A clear description of statistics including <u>central tendency</u> (e.g. median, mean) and <u>variation</u> (e.g. standard deviation, interquartile range)  |
| <input type="checkbox"/>            | <input checked="" type="checkbox"/> Clearly defined error bars   |

See the web collection on [statistics for biologists](#) for further resources and guidance.



## ► Software

Policy information about [availability of computer code](#)

### 7. Software

Describe the software used to analyze the data in this study.

GraphPad Prism 6 for Mac, Adobe Photoshop CC, AMIDE Medical Image Data Examiner 1.0.4

For manuscripts utilizing custom algorithms or software that are central to the paper but not yet described in the published literature, software must be made available to editors and reviewers upon request. We strongly encourage code deposition in a community repository (e.g. GitHub). *Nature Methods* [guidance for providing algorithms and software for publication](#) provides further information on this topic.

## ► Materials and reagents

Policy information about [availability of materials](#)

### 8. Materials availability

Indicate whether there are restrictions on availability of unique materials or if these materials are only available for distribution by a for-profit company.

V-9302 was synthesized at Vanderbilt University and can be made available upon request. The patient-derived xenograft (PDX) described in this study was generated at Vanderbilt University Medical Center and may have limited generational availability as the tissue is used in further studies.

### 9. Antibodies

Describe the antibodies used and how they were validated for use in the system under study (i.e. assay and species).

Antibodies used for immuno blot: ASCT2 - Millipore-Sigma (ABN73); ASCT1 - Cell Signaling Technology (8442); Tubulin - Novus Biologicals (NB600-936); phospho-S6 Ribosomal Protein - Cell Signaling Technology (4858S); S6 Ribosomal Protein - Cell Signaling Technology (2217S); phospho-p44/42 (Erk1/2) - Cell Signaling Technology (4376S); p44/42 MAPK (Erk1/2) - Cell Signaling Technology (4695S); Caspase-3 - Cell Signaling Technology (9662). Antibodies used for immunofluorescence: LC3B - Cell Signaling Technology (2775); AKT1 (phospho S473) - Abcam (ab81283); BRDU - ThermoFisher Scientific (03-3900); Secondary antibody Rhodamine Red - ThermoFisher Scientific (R-6393, R-6394)

### 10. Eukaryotic cell lines

a. State the source of each eukaryotic cell line used.

All cells lines were obtained from commercial vendors (ATCC) or provided by other laboratories at Vanderbilt.

b. Describe the method of cell line authentication used.

All immortalized cell lines were authenticated using a commercial vendor (Genetica DNA Laboratories).

c. Report whether the cell lines were tested for mycoplasma contamination.

All cell lines used tested negative for mycoplasma contamination.

d. If any of the cell lines used are listed in the database of commonly misidentified cell lines maintained by [ICLAC](#), provide a scientific rationale for their use.

The cell lines MCF-7 and H460, which can be found on the ICLAS list of commonly misidentified cell lines were used in the in vitro studies. These cell lines have been used commonly in our lab and were validated prior to use in these studies.

## ► Animals and human research participants

Policy information about [studies involving animals](#); when reporting animal research, follow the [ARRIVE guidelines](#)

### 11. Description of research animals

Provide details on animals and/or animal-derived materials used in the study.

All mice used in these studies were 5-6 week old female Hsd:Athymic Nude-Foxn1nu mice from Envigo.

Policy information about [studies involving human research participants](#)

### 12. Description of human research participants

Describe the covariate-relevant population characteristics of the human research participants.

This study did not involve human research participants.

## Flow Cytometry Reporting Summary

Form fields will expand as needed. Please do not leave fields blank.

### ▶ Data presentation

For all flow cytometry data, confirm that:

- 1. The axis labels state the marker and fluorochrome used (e.g. CD4-FITC).
- 2. The axis scales are clearly visible. Include numbers along axes only for bottom left plot of group (a 'group' is an analysis of identical markers).
- 3. All plots are contour plots with outliers or pseudocolor plots.
- 4. A numerical value for number of cells or percentage (with statistics) is provided.

### ▶ Methodological details

- |  |  |
|--|--|
| 5. Describe the sample preparation.  | HCC1806 and HT29 cells (ATCC) were treated with V-9302 (48h) followed by incubation with 5 uM CM-H2DCFDA for 60 min according to the manufacturers protocol.   |
| 6. Identify the instrument used for data collection.                                   | BD LSRII S/N H1001   |
| 7. Describe the software used to collect and analyze the flow cytometry data.          | BD FACSDiva software v 8.0.1   |
| 8. Describe the abundance of the relevant cell populations within post-sort fractions. | These cells were not sorted  |
| 9. Describe the gating strategy used.  | The cells were identified by their FSC and SSC profiles. A polygon gate was drawn on a FSC-A vs SSC-A dot plot to include the cell population. Aggregates were identified and removed from the analyzed population by SSC-W vs SSC-H doublet discrimination gates; followed by FSC-W vs FSC-H doublet discrimination gates. The boundaries between positive and negative gates were set based upon an unstained control. |

Tick this box to confirm that a figure exemplifying the gating strategy is provided in the Supplementary Information.